Supporting Information for

An ultra-sensitive ethene detector based on a graphene-copper(I) hybrid material

Wangyang Fu,[1†] Thomas F. van Dijkman,[2†] Lia M.C. Lima,[1] Feng Jiang,[2] Grégory F. Schneider,[1]* and Elisabeth Bouwman[2]*

[1] *Supramolecular & Biomaterials Chemistry, Leiden University, Leiden Institute of Chemistry, PO Box 9502, 2300 RA Leiden, The Netherlands*

[2] *Metals in Catalysis, Biomimetics & Inorganic Materials; Leiden University, Leiden Institute of Chemistry, PO Box 9502, 2300 RA Leiden, The Netherlands*

* to whom correspondence should be addressed: g.f.schneider@lic.leidenuniv.nl, +31 71 527 2700; bouwman@chem.leidenuniv.nl, +31 71 527 4550

† equal contribution

This PDF file includes:

section S1. Synthesis and characterizations of the complexes

The sodium hydridotrispyrazolylborate ligand (1.00 g, 1.14 – 1.38 mmol) was dissolved in dichloromethane (50 mL) or toluene (50 mL, only used in the case of $NaTp^{CF3,4F-Ph}$) and the solution was purged with argon to remove dissolved dioxygen. After bubbling for five minutes $[Cu(MeCN)_4]SbF_6$ (1.0 equivalent) was added. The solution was left to stir under argon overnight. The following day the stirring was stopped to allow the $NaSbF_6$ by-product to settle. The supernatant was then siphoned off and filtered through a syringe filter (0.45 μm, PTFE). The clear solutions were evaporated to dryness in vacuo to yield the complexes as white solids. The complexes thus obtained were typically of good purity, additional purification could be performed by recrystallization of the complexes using DCM/Et_2O, DCM/pentane or storage of a concentrated solution of a complex in DCM at –20 °C.

[Cu($Tp^{CF3,4CF3-Ph}$)(MeCN)], Performed using half amounts of all compounds, yield 381 mg (87%). ^{1}H NMR (500 MHz, CD_2Cl_2) δ 7.21 (d, J = 8.3 Hz, 6H), 6.98 (d, J = 8.3 Hz, 6H), 6.61 (s, 3H), 4.37 (bs, 1H), 2.32 (s, 3H). ^{19}F NMR (471 MHz, CD_2Cl_2) δ –61.84, –63.48. ^{13}C NMR (126 MHz, CD_2Cl_2) δ 148.66, 142.49 (q, J = 37.8 Hz), 134.68, 131.02 (q, J = 33.1 Hz), 130.46, 124.99, 124.13 (q, J = 272.0 Hz), 121.53 (q, J = 269.3 Hz), 114.55, 105.10, 2.70. Analysis (calcd., found for $C_{35}H_{19}BCuF_{18}N_7 \cdot 1.5H_2O \cdot 0.5Et_2O$): C (43.66, 43.36), H (2.67, 2.78), N (9.63, 9.36).

[Cu($Tp^{CF3,4Cl-Ph}$)(MeCN)], Yield 963 mg (95%). ^{1}H NMR (500 MHz, CD_2Cl_2) δ 7.01 (d, J = 8.4 Hz, 6H), 6.79 (d, J = 8.4 Hz, 6H), 6.54 (s, 3H), 4.38 (bs, 1H), 2.30 (s, 3H). ^{19}F NMR (471 MHz, CD_2Cl_2) δ –61.89. ^{13}C NMR (126 MHz, CD_2Cl_2) δ 157.30, 148.98, 142.23 (q, J = 37.4 Hz), 135.10, 131.40, 129.56, 128.34, 121.61 (q, J = 269.4 Hz), 114.41, 104.65 (q, J = 1.7 Hz), 2.70. Analysis (calcd., found for $C_{32}H_{19}BCl_3CuF_9N_7 \cdot 0.1DCM$): C (44.74, 44.48), H (2.25, 2.42), N (11.38, 11.18).

[Cu($Tp^{CF3,4F-Ph}$)(MeCN)], Yield 635 mg (63%). ^{1}H NMR (500 MHz, CD_2Cl_2) δ 6.87 (ddd, J = 8.2, 5.2, 2.5 Hz, 6H), 6.73 (t, J = 8.7 Hz, 6H), 6.52 (s, 2H), 2.30 (s, 3H). ^{19}F NMR (471 MHz, CD_2Cl_2) δ –61.88, -113.25 (tt, J = 8.8, 4.7 Hz). ^{13}C NMR (126 MHz, CD_2Cl_2) δ 149.14, 144.43, 131.90 (d, J = 8.4 Hz), 127.24, 115.04 (d, J = 22.0 Hz), 104.72 (q, J = 2.0 Hz), 1.15. Some resonances were not observed as a result of the low solubility of the compound and splitting caused by the fluoro substituents. Analysis (calcd., found for $C_{32}H_{19}BCuF_{12}N_7 \cdot 0.7DCM \cdot 0.5$toluene): C (47.81, 48.22), H (2.70, 2.52), N (10.78, 10.37).

[Cu(Tp^{CF3-Ph})(MeCN)], Yield 897 mg (87%). ^{1}H NMR (500 MHz, CD_2Cl_2) δ 7.28 (dd, J = 8.1, 6.5 Hz, 3H), 6.95 (t, J = 7.6 Hz, 6H), 6.92 (dd, J = 7.9, 1.4 Hz, 6H), 6.55 (s, 3H), 4.66 (bs, 1H), 2.30 (s, 3H). ^{19}F NMR (471 MHz, CD_2Cl_2) δ –61.76. ^{13}C NMR (126 MHz, CD_2Cl_2) δ 151.88, 150.44, 141.99 (q, J = 37.3 Hz), 131.07, 130.06, 128.61, 128.18, 121.89 (q, J = 269.0 Hz), 114.32, 104.53 (q, J = 1.8 Hz), 2.69. Analysis (calcd., found for $C_{32}H_{22}BCuF_9N_7$): C (51.25, 51.11), H (2.96, 3.11), N (13.07, 12.73).

[Cu(Tp$^{CF3,4OMe-Ph}$)(MeCN)], Yield 997 mg (97%). ^{1}H NMR (500 MHz, CD_2Cl_2) δ 6.84 (d, J = 8.7 Hz, 6H), 6.55 (d, J = 8.7 Hz, 6H), 6.52 (s, 3H), 4.56 (bs, 1H), 3.82 (s, 9H), 2.33 (s, 3H). ^{19}F NMR (471 MHz, CD_2Cl_2) δ –61.67. ^{13}C NMR (126 MHz, CD_2Cl_2) δ 160.08, 150.14, 141.81 (q, J = 37.0 Hz), 131.47, 122.94, 121.87 (q, J = 268.6 Hz), 113.42, 103.97, 55.43, 2.69. Analysis (calcd., found for $C_{35}H_{28}BCuF_9N_7O_3$): C (50.05, 49.99), H (3.36, 3.31), N (11.67, 11.61).

[Cu(Tp$^{CF3,4NMe2-Ph}$)(MeCN)], Yield 863 mg (84%). ^{1}H NMR (500 MHz, CD_2Cl_2) δ 6.77 (d, J = 8.8 Hz, 6H), 6.47 (s, 2H), 6.30 (d, J = 8.8 Hz, 6H), 4.73 (s, 1H), 2.95 (s, 18H), 2.32 (s, 3H). ^{19}F NMR (471 MHz, CD_2Cl_2) δ –61.61. ^{13}C NMR (126 MHz, CD_2Cl_2) δ 150.98, 150.40, 141.51 (q, J = 37.3 Hz), 130.96, 125.20, 122.00 (q, J = 268.8 Hz), 114.08, 111.44, 103.29, 40.17, 2.73. Analysis (calcd., found for $C_{38}H_{37}BCuF_9N_{10}\cdot 0.5C_5H_{12}$): C (53.15, 53.30), H (4.74, 4.26), N (15.30, 15.59)

All reflection intensities were measured at 110(2) K using a SuperNova diffractometer (equipped with Atlas detector) with Mo *K*α radiation (λ = 0.71073 Å) under the program CrysAlisPro (Version 1.171.36.32 Agilent Technologies, 2013). The temperature of the data collection was controlled using the system Cryojet (manufactured by Oxford Instruments). CrysAlisPro program was used to refine the cell dimensions and for data reduction. The structure was solved by direct methods with SHELXS-2014/7 (Sheldrick, 2015) and was refined on F^2 with SHELXL-2014/7 (Sheldrick, 2015). Analytical numeric absorption correction based on a multifaceted crystal model was applied using CrysAlisPro. The H atoms were placed at calculated positions (unless otherwise specified) using the instructions AFIX 43 or AFIX 137 with isotropic displacement parameters having values 1.2 or 1.5 *U*eq of the attached C atoms. The H atoms attached to B1 was found from difference Fourier map, and its coordinates and isotropic temperature factor were refined freely. The structure is partly disordered, two of the three $-CF_3$ groups are found to be disordered over either two or three orientations. For the less disordered $-CF_3$ group, the occupancy factor of the major component of the disorder refines to 0.77(2). For the more disordered $-CF_3$ group, the three occupancy factors refine to 0.275(3) 0.394(3) and 0.331(3). The sum of those three occupancy factors was restrained to be 1 using the SUMP restraint. CCDC 1546427 contains the supplementary crystallographic data for the complex.

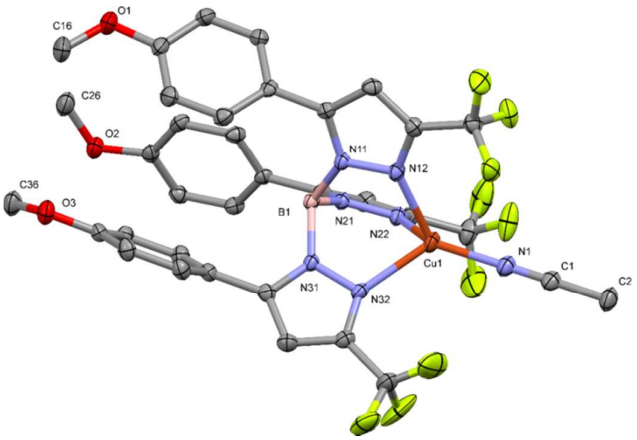

Figure S1. Projection of the structure of [Cu(Tp$^{CF3,4\text{-}OMePh}$)(MeCN)] with ellipsoids plotted at the 50% probability level. Hydrogen atoms have been omitted for the sake of clarity. Selected distances (Å) and angles (°): B1···Cu1 3.057(2), Cu1–N12 2.0772(14), Cu1–N22 2.0745(14), Cu1–N32 2.1096(14), Cu1–N1 1.8813(14), N1–C1 1.136(2), Cu1–N1–C1 179.23(16), N12–Cu1–N32 92.50(5), N12–Cu1–N1 124.33(6). The complex has approximate three-fold rotational symmetry that is broken by varying degrees of rotation of the phenyl rings with respect to the pyrazole rings; the dihedral angles between the phenyl and the pyrazole rings are 46.0(2)°, 55.7(2)° and 60.6(2)°. The differences in the observed distances in the ethene, carbonyl and acetonitrile complexes are likely attributable at least in part to crystal packing effects. Similarly, the different dihedral angles between the phenyl rings and the pyrazoles are most likely caused by π-stacking in the crystal lattice as the rings have some rotational freedom.

Table S1. Crystal data for [Cu($Tp^{CF3,4\text{-}OMe\text{-}Ph}$)(MeCN)].	
Chemical formula	$C_{35}H_{28}BCuF_9N_7O_3$
CCDC	1546427
M_r	839.99
Crystal system, space group	Monoclinic, $P2_1/n$
Temperature (K)	110
a, b, c (Å)	14.9284 (4), 11.1160 (3), 22.1547 (7)
β (°)	102.349 (3)
V (Å^3)	3591.38 (18)
Z	4
Radiation type	Mo $K\alpha$
μ (mm^{-1})	0.70
Crystal size (mm)	0.43 × 0.37 × 0.34
Data collection	
Diffractometer	SuperNova, Dual, Cu at zero, Atlas diffractometer
T_{min}, T_{max}	0.790, 0.838
No. of measured, independent and observed [$I > 2\sigma(I)$] reflections	27839, 8255, 7045
R_{int}	0.024
$R[F^2 > 2\sigma(F^2)]$, $wR(F^2)$, S	0.034, 0.083, 1.03
No. of reflections	8255
No. of parameters	598
No. of restraints	115
H-atom treatment	H atoms treated by a mixture of independent and constrained refinement
$\Delta\rho_{max}$, $\Delta\rho_{min}$ (e Å^{-3})	0.33, –0.38

Computer programs: *CrysAlis PRO*, Agilent Technologies, Version 1.171.36.32 (release 02-08-2013 CrysAlis171 .NET) (compiled Aug 2 2013, 16:46:58), *SHELXS2014*/7 (Sheldrick, 2015), *SHELXL2014*/7 (Sheldrick, 2015), *SHELXTL* v6.10 (Sheldrick, 2008).

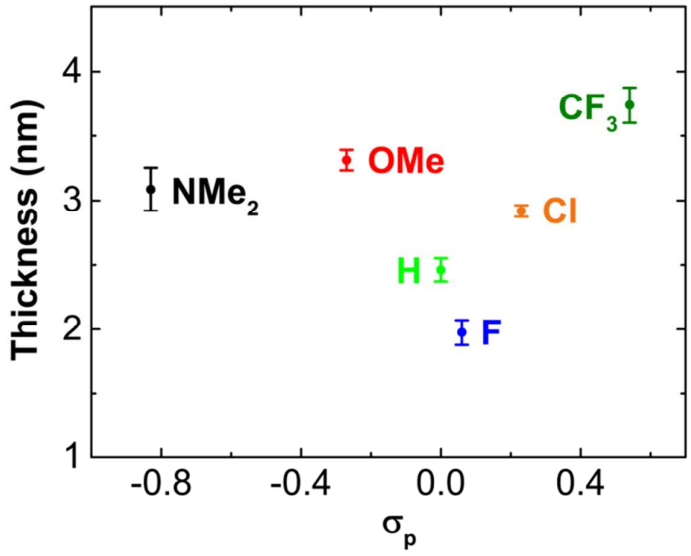

Figure S2. Average thicknesses of the adsorbed Cu complex layers on graphene as determined by ellipsometry. Note that the thinnest layer is of *R* = F which was the only complex that was not soluble enough to form a 10 mM solution in DCM.

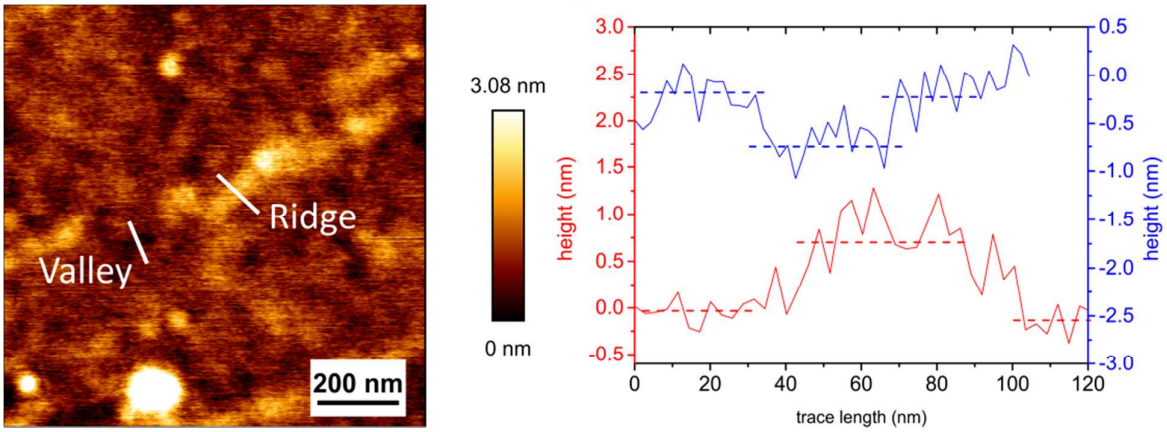

Figure S3. AFM image of the surface of [Cu(Tp$^{CF3,4\text{-}OMePh}$)(MeCN)] on graphene. The height traces on the right show the valley (blue) and the ridge (red) indicated in the image, the observed step heights correspond with monolayers.

To study the physical effects of gas exposure to a device, a collection of devices was characterized by AFM before and immediately after exposure to ethene gas. The device surfaces in all cases remained as featureless, or even more so, as before exposure (see Figure S4-6). In a control experiment with the reference complex [Cu(Tp$^{(CF3)2}$)(MeCN)] on HOPG, small monolayer islands (formed by drop casting a dilute solution of the complex) showed clear signs of fluidization upon exposure to ethene as a non-crystalline mixture of complexes forms when the complexes react with the gas (see Figure S4). We believe a similar effect is responsible for both the featureless nature of the observed surfaces and the good reactivity towards the analyte gases.

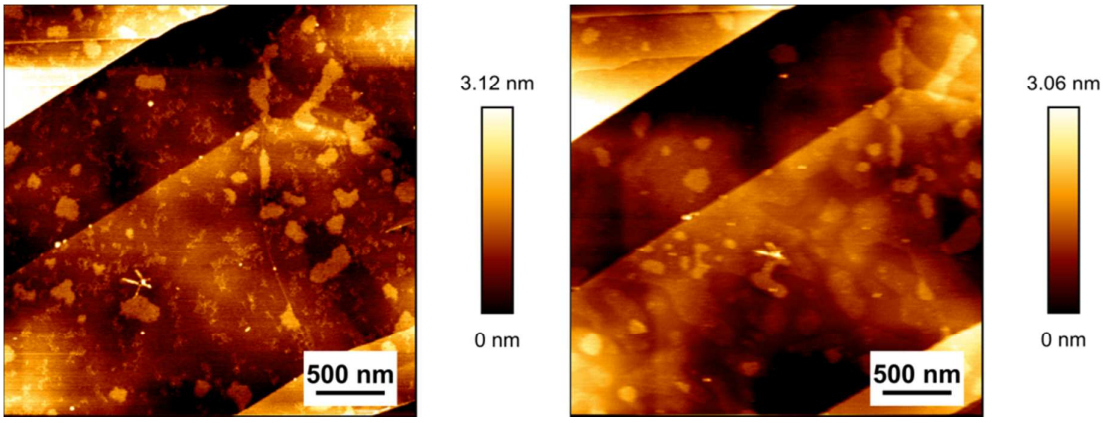

Figure S4. AFM images of [Cu(Tp$^{(CF3)2}$)(MeCN)] on HOPG. The complex forms large domains of monolayers (left). On the right the same area is shown after exposure to ethene gas. The features on the surface show signs of diffusion.

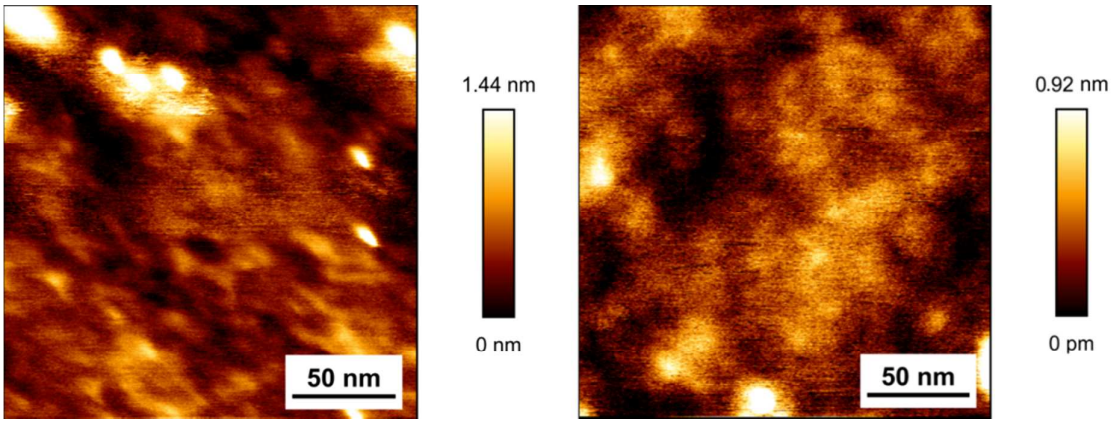

Figure S5. AFM image of [Cu(Tp$^{CF3,4\text{-}CF3Ph}$)(MeCN)] on graphene before (left) and after (right) ethene exposure. Not the same location on the sample.

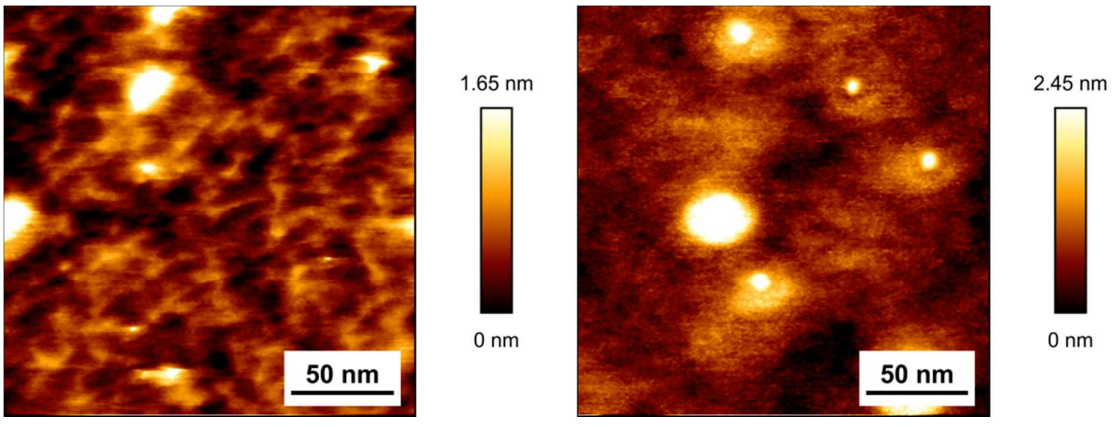

Figure S6. AFM images of [Cu(Tp$^{CF3,4\text{-}FPh}$)(MeCN)] before (left) and after (right) exposure to ethene gas on graphene. Not the same location on the sample.

We have recorded and compared the Raman spectra of the complexes (*R* = OMe, with MeCN and CO ligands) in bulk crystalline material as well as on the surface of graphene after drop-casting and self-assembly, and after 4 days of storage in ethene at 20 ppm (see Figure S7). We adopted drop-casting instead of dip coating to achieve a better Raman signal of the molecules on the surface of graphene. Our Raman data confirm that the compounds are intact on graphene:

In Figure S7a the Raman spectra are shown of complexes (*R* = OMe with MeCN and CO ligands) in bulk crystalline material (black curves, each averaged over 3 spots) and after drop-casting on graphene after self-assembly (red curves). Beside the G and 2D Raman peaks of graphene (at 1594 and 2685 cm^{-1}, respectively), a typical Raman spectrum of the self-assembled complex (*R* = OMe, with MeCN and CO ligand) on graphene contains well-defined Raman peaks, which are comparable to those of the corresponding bulk materials (at 1443, 1453, 1616, and 2287 cm^{-1} for the MeCN ligand and at 1443, 1453, 1616, and 2096 cm^{-1} for the CO ligand). Thus we confirmed the stability of these self-assembled complexes on graphene by the presence of the Raman peaks as identified from their bulk materials (black curves, Figure S7a).

In Figure S7b a zoom-in around the G peak of graphene is shown of the Raman spectra of the complex (*R* = OMe with MeCN ligand) in bulk material (black curve) and on graphene after self-assembly (red curve). We observed that the Raman spectrum of the complex on graphene is rather stable and did not change much even after 4 days of storage in ethene (blue curve, Figure S7b).

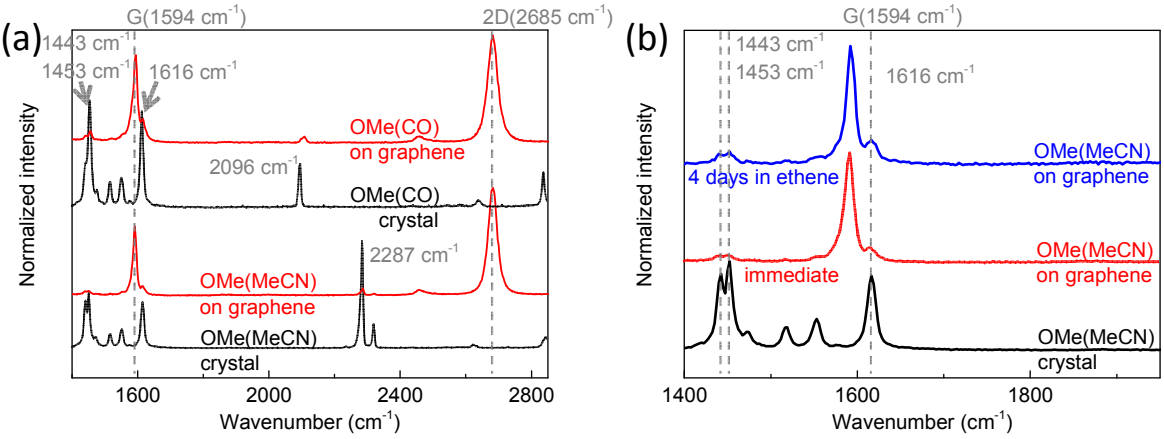

Figure S7. Raman spectra of the complexes (*R* = OMe), with (a) CO and (b) MeCN ligands, in bulk material and on the surface of graphene after solution process and self-assembly, confirming the stability of the complexes on graphene.

section S2. High-performance GFET on SiO_2/Si with OTS-SAM functionalization

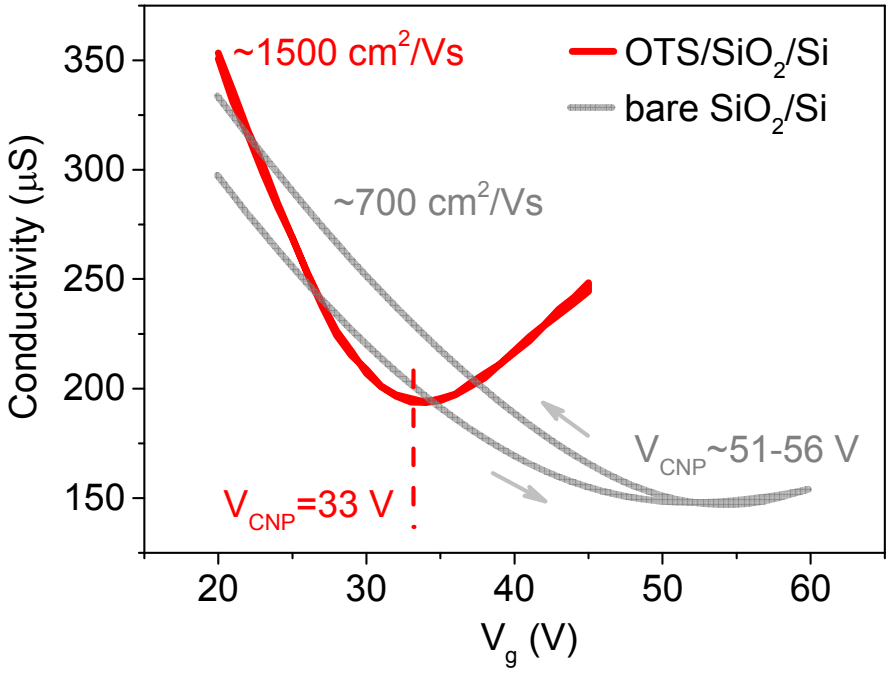

Figure S8. The back gate voltage (V_g) dependent conductivity (G) of graphene on bare SiO_2/Si substrate (gray) and on organic molecule octadecyltrichlorosilane (OTS) modified SiO_2/Si substrate (red).

The graphene device on bare SiO_2/Si substrate exhibit a hysteresis of 5 V with an average charge neutrality point (CNP) V_{CNP} ~ +53.5 V (Figure S8). The relatively large hysteresis and V_{CNP} can be ascribed to the well-known p-doping effect of the SiO_2/Si substrate. Apparently, the OTS helps to screen the substrate effect. As a result, the electrical performances of the graphene devices is improved with negligible hysteresis loop and a small V_{CNP} (33 V). We note here that the estimated hole carrier mobility of graphene increases on OTS (~1500 cm^2/Vs compared to ~700 cm^2/Vs on bare substrate) is most likely come from the high quality of graphene on this ultra-smooth organic self-assembled monolayer (SAM)-modified platform [*Nano Lett.*, **2012**, 12, 964–969]. The high-performance graphene transistors on our solution-processable OTS/SiO_2/Si substrates are crucial for our development of ultrasensitive graphene gas sensors with reproducible performance.

section S3. Life-time of GFET with copper(I) complexes

We have studied in-depth the lifetimes of the devices with the complex (R = OMe) and complex (R = CF_3). Depicted in Figure S9 are their (relative) sensing response (to ethene at 1 ppm) over a testing period of 12 days. The sensing behaviors of the devices are stable over 12 days (within a maximum deviation of $\Delta V_G/\Delta V_{G0} < 40\%$), suggesting a good air stability of the copper(I) complexes and the assembled devices. The baseline-corrected trace of the response of GFET (R = OMe) exposed to ethene at 1 ppm (after 12 days of operation) is shown in the inset of Figure S9.

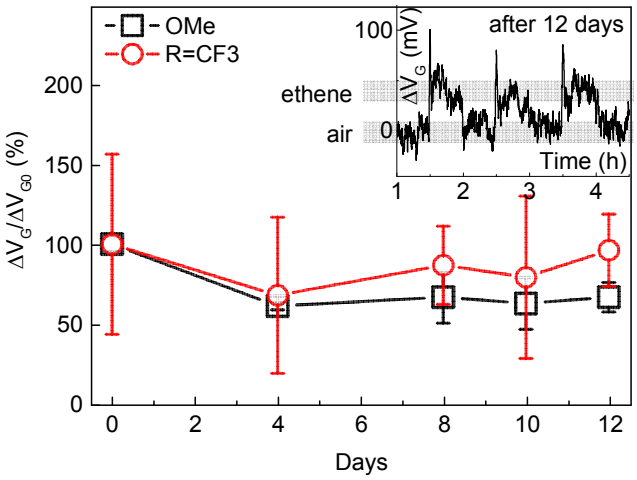

Figure S9. Sensing stability of the devices (to ethene at 1 ppm) with complex (R = OMe) and complex (R = CF_3) over a testing period of 12 days. Inset: baseline-corrected trace of the response of GFET (R = OMe) exposed to ethene at 1 ppm after 12 days of operation.

section S4. Gate potential due to 2D array of dipoles

The dipole moments found in the mononuclear Cu complexes (Figure 4 in the main text) exist because of the non-uniform distribution of electron density across the atoms of the complex. Dipole moments can be expressed as $\vec{D} = Q\vec{d}$, a vector quantity given by the strength of each charge Q multiplied by the separation between the charges $\vec{d}$. Any organization of n dipolar molecules (*i.e.* self-assembly on a 2D surface or crystallization) results in a polarization density $\overrightarrow{D_n}$. In a situation without intermolecular interactions the dipoles would be randomly oriented leading to a zero polarization density $\overrightarrow{D_n}$. However, the π-π interactions between the phenyl rings in the complexes and the graphene surface as well as polar interactions between the Cu complexes facilitate self-assembly which is why Cu complexes adsorbed to graphene are expected to have a non-zero out-of-plane polarization density $D_{n\perp}$. The influence of the layers that lie atop the layer that is in direct interaction with the graphene likely contribute to the out-of-plane polarization density in a considerably smaller degree than the first layer. This follows from the trends observed in the main text (*e.g.* in Figure 3a) which show no correlation between signal the intensity ΔV_G and the layer thickness.

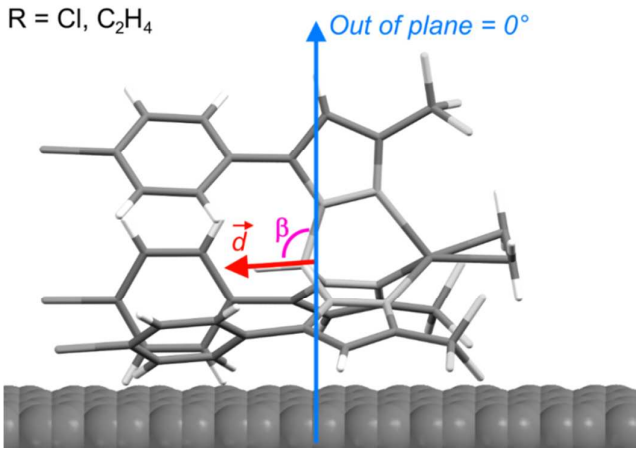

Figure S10. Illustration of the orientation of an ethene complex (R = Cl) on graphene with the dipole vector in red, the normal angle of the graphene in blue and the angle β_{ave} in purple.

The out-of-plane polarization density can be described as $D_{n\perp} = \mathrm{n}D\cos\beta_{ave}$; n is the surface density of the 2D array, β_{ave} is defined as the average angle between the dipoles and the out-of-plane direction: $\cos\beta_{ave} = \frac{1}{N}\sum_1^N \cos\beta$, $N \to \infty$ is the total number of molecules in the 2D array.

Using Gauss's Law: the total of the electric flux out of a closed surface (in our case the out-of-plane electric field $E_\perp$ multiplied by the area of the surface projected in a plane perpendicular: S) is equal to the charge enclosed divided by the permittivity. Using an infinite parallel plate approximation (ignoring the fringes as the nanometer thickness of the Cu complex layer is much smaller than the millimeter size of the graphene flake) the uniformly distributed electric field can be calculated: $E_\perp = \frac{D_{n\perp}}{d\varepsilon}$ where ε is the permittivity of the Cu complex. We assume the complexes have a low permittivity (*i.e.* $\varepsilon \sim 3-5\varepsilon_0$, ε_0 is the vacuum

permittivity), a relatively small value as the complexes are anchored to the graphene surface via π-π interactions and thus unable to contribute significantly to the permittivity of the system by tumbling. In conclusion, the gate potential induced in graphene due to 2D array of dipoles of the Cu complex can be approximated by using Equation S1:

$$U = E_{\perp}\mathrm{d} = \frac{D_{n\perp}}{\varepsilon} = \frac{\mathrm{n}D\cos\beta_{ave}}{\varepsilon} \quad \text{(S1)}$$

From which the angle β_{ave} can be extracted using Equation S2:

$$\beta_{ave} = \cos^{-1}\frac{\varepsilon\Delta U}{\mathrm{n}\Delta D} \quad \text{(S2)}$$

As an estimation of the order of magnitude of the average angle (β_{ave}) for the representative case of R = NMe_2 with C_2H_4 Equation S2 was applied using $\mathrm{n} = 2.5 \times 10^{17}\mathrm{m}^{-2}$ (the approximate surface density of the first Cu complex layer directly on top of the graphene), $\varepsilon = 4\,\varepsilon_0$, $\Delta U = 0.1\,V$ (Figure 3a) and $\Delta D = 15$ D (Figure 4b). We obtain $\beta_{ave} \sim 99^{\circ}$ which is in good agreement with our expectation that the Cu complex should be aligned more or less parallel to the graphene surface due to π-stacking interactions. The induced gate potential does not depend on the distance between the Cu complex dipolar layer and the graphene surface, this is valid as far as the infinite parallel plate approximation is correct which is the case as long as the thickness of the Cu complex layer is much smaller than the size of the graphene flake and the fringes can be ignored. Nevertheless, due to the sophisticated nature of the interaction and the limited information we have with respect to the microscopic arrangement of the complexes and the local graphene environment, this phenomenological model was applied for order-of-magnitude estimations at its best.

section S5. Data processing

Data processing for the signals obtained from the gas exposure experiments requires a number of steps that are visually outlined in Figure S11.

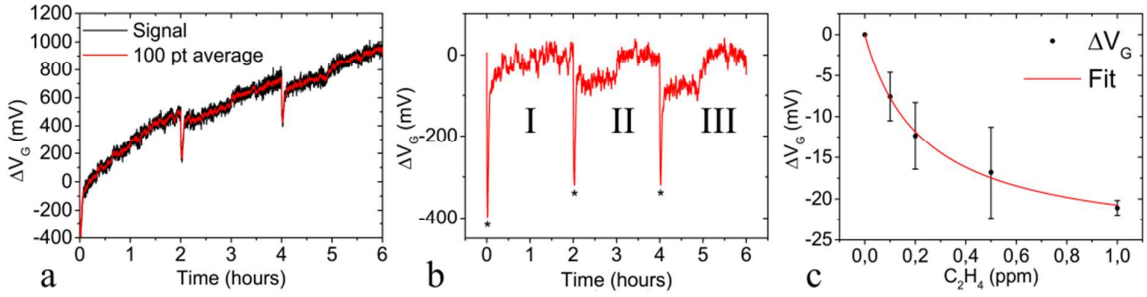

Figure S11. a. Plot of the raw signal from a GFET device (black) over the course of three consecutive cycles of exposure to ethene and air after being normalized using the device transconductance. At this point in data processing the signal is still convoluted with noise and drift. To limit the influence of noise the floating average over 100 points (red) is sometimes useful. Averaging is typically only required in case of poor signal to noise ratios. **b.** The same (100-point-averaged) signal is shown as in **a** but with the baseline drift subtracted. The signal is still convoluted with noise, in some cases the drift in the baseline is too great to extract useful data, signal I is an example of such a signal. Such signals are not used. Signals II and III have the expected line shape and show clear steps when exposure to ethene gas is initiated or halted. When ethene gas is applied a pressure spike (caused by the MFCs) is clearly visible. In order to exclude the influence of the MFCs gas exposures were continued for a period of one hour during which the signal stabilized. Upon cessation of exposure the signal returns to the baseline, this step height is taken as the signal intensity. **c.** The averaged response intensities at different concentrations of ethene gas are shown *vs*. the ethene concentrations. The red line is a fit using a Langmuir Isotherm from which K_D and the prefactor $(\frac{D_{n^{\perp}}}{\varepsilon})["on"]_{max}$ are extracted.

Table S1. GFET responses to different ethene concentrations (ppm) for the different substituents R on the ligand

	Cl		F		H	
[C_2H_4] (ppm)	ΔV_G	S.E.	ΔV_G	S.E.	ΔV_G	S.E.
1	102.8	9.8	64.6	1.6	-21.1	0.9
0.5	73.2	4.1	69.8	0.3	-16.8	5.5
0.2	76.6	8.2	76.0	0.8	-12.4	4.1
0.1	26.5	13	61.7	3.2	-7.6	3.0
0	0.0	-	0.0	-	0.0	-
	OMe		NMe_2		$(CF_3)_2$	
[C_2H_4] (ppm)	ΔV_G	S.E.	ΔV_G	S.E.	ΔV_G	S.E.
1	-54.8	4.7	-98.7	8.3	101.6	16
0.5	-62.6	5.8	-76.0	4.3	37.8	4.2
0.2	-63.6	11	-61.1	5.8	16.2	2.0
0.1	-54.7	8.9	-	-	8.7	-
0	0.0	-	0.0	-	0.0	-

Table S2. GFET responses to different ethanol concentrations (ppm) for the different substituents R on the ligand.

[Ethanol] (ppm)	Cl		F		H	
	ΔV_G	S.E.	ΔV_G	S.E.	ΔV_G	S.E.
10	92.5	4.8	48.9	4.4	-24.4	11
5	71.4	13	30.2	3.2	-12.1	0.46
2	53.9	7.2	20.7	0.93	-3.9	0.18
1	15.0	5.0	21.4	2.0	7.0	-
0	0.0	0.0	0.0	0.0	0.0	0.0
[Ethanol]	OMe		NMe2		$(CF_3)_2$	

(ppm)	ΔV_G	S.E.	ΔV_G	S.E.	ΔV_G	S.E.
10	-77.1	24	-129.6	14	-327.9	1.6
5	-24.6	19	-127.2	12	-58.4	-
2	-27.3	4.0	-60.1	11	-41.6	2.5
1	-	-	-	-	-	-
0	0.0	-	0.0	-	0.0	-

Table S3. Prefactors (from Eq. 1 in the main text), equilibrium dissociation constants and k_{-1} extracted from the transconductance-corrected signals obtained when the GFET devices were exposed to ethanol vapor.

R	σ_p	prefactor		K_D		k_{-1} ($\times 10^{-3}$)	
		mV	S.E.	ppm	S.E.	s^{-1}	S.E.
NMe_2	-0.83	-181	20	3.15	0.95	11	4.0
OMe	-0.27					8.3	1.5
H	0	-4.72	0.95	0.44	0.55	13	2.1
F	0.06	59.1	7.1	3.13	0.95	17	0.88
Cl	0.23	129	12.5	3.91	0.9	25	1.7

Table S4. Prefactors (from Eq. 1 in the main text), equilibrium dissociation constants and k_{-1} extracted from the transconductance-corrected signals obtained when the GFET devices were exposed to ethene gas.

R	σ_p	prefactor		K_D		k_{-1} ($\times 10^{-3}$)	
		mV	S.E.	ppm	S.E.	s^{-1}	S.E.
NMe_2	-0.83	-96.9	4.9	0.11	0.034	8.1	0.89
OMe	-0.27	-60.3	2.0	0.0052	0.0061	3.9	0.26
H	0	-25.5	0.5	0.23	0.026	7.9	0.27
F	0.06					9.9	0.75
Cl	0.23	119.6	12.7	0.21	0.066	15	0.76
CF_3	0.54	95.8	9.1				

section S6. DFT-optimized structures

The Amsterdam Density Functional (ADF) program with DFT at the level of ZORA-OPBE/QZ4P was employed for all the calculations. Geometry optimizations for [CuTp$^{CF3,4-CF3Ph}$)], [CuTp^{CF3,Ph})] and [CuTp$^{CF3,4-NMe2Ph}$)] were conducted with C_3 symmetry; the geometry optimizations for [CuTp$^{CF3,4-CF3Ph}$)(C_2H_4)], [CuTp^{CF3,Ph})(C_2H_4)] and [CuTp$^{CF3,4-NMe2Ph}$)(C_2H_4)] were carried out with C_1 symmetry. All calculations were performed in the gas phase.

Table S5. Absolute magnitudes of the dipole moments as calculated for the ethene and ethanol complexes for *R* = NMe_2, H and CF_3 and their respective mononuclear and dinuclear proposed resting states. (unit: Debye)

R	**CF_3**	**H**	**NMe_2**
[Cu(Tp^{CF3,RPh})]	0.49948474	7.71935672	16.25651267
[Cu(Tp^{CF3,RPh})]$_2$	0.76231604	0.16735481	0.19678718
[Cu(Tp^{CF3,RPh})(C_2H_4)]	1.90391701	6.62530646	15.01153011
[Cu(Tp^{CF3,RPh})(C_2H_5OH)]	4.88608573	5.61705720	11.89985192

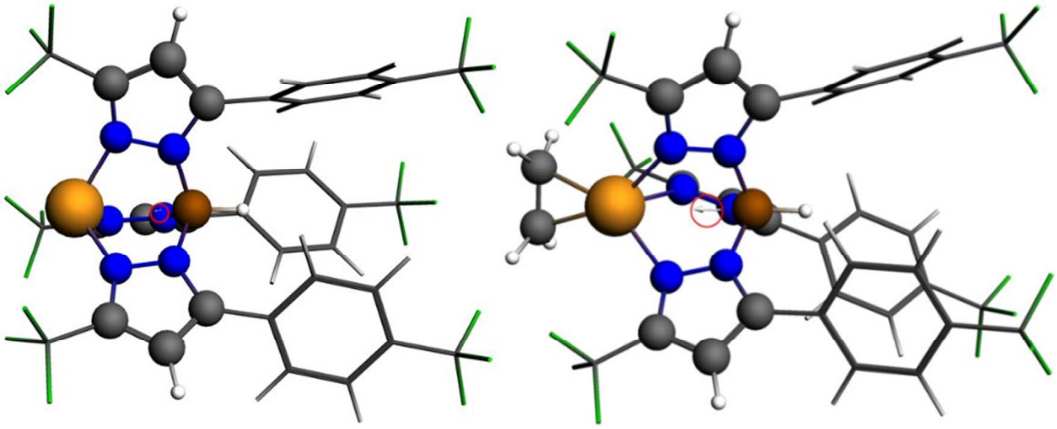

Figure S12. Projection of the structure of [Cu(Tp$^{CF3,4-CF3Ph}$)] (left) and [Cu(Tp$^{CF3,4-CF3Ph}$)(C_2H_4)] (right) after geometry optimization at the ZORA-OPBE/QZ4P level of theory in vacuum. Parts of the molecule are shown as wireframes for the sake of clarity; the dipole vector is circled in red.

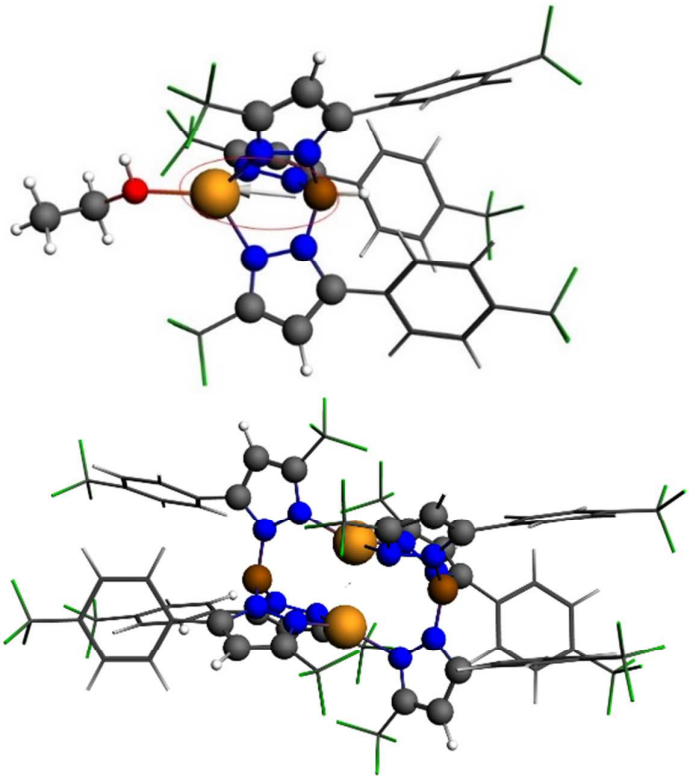

Figure S13. Projection of the structure of [Cu($Tp^{CF3,4\text{-}CF3Ph}$)(C_2H_5OH)] (left) and [Cu($Tp^{CF3,4\text{-}CF3Ph}$)]$_2$ (right) after geometry optimization at the ZORA-OPBE/QZ4P level of theory in vacuum. Parts of the molecule are shown as wireframes for the sake of clarity; the dipole vector in the ethanol complex is circled in red, note the very small dipole vector in the dinuclear complex on the right.

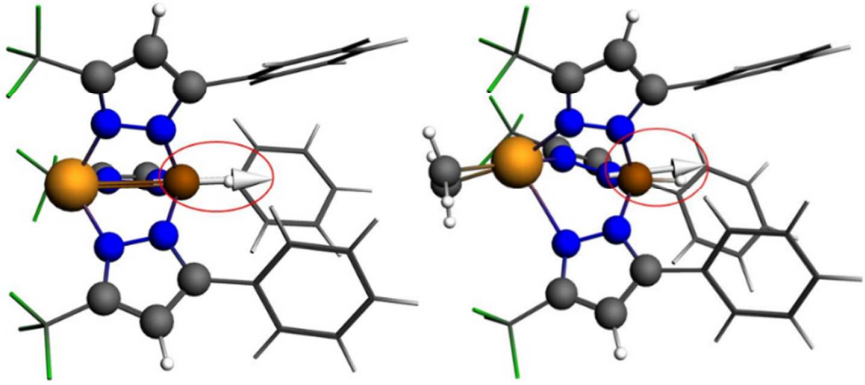

Figure S14. Projection of the structure of [Cu($Tp^{CF3,Ph}$)] (left) and [Cu($Tp^{CF3,Ph}$)(C_2H_4)] (right) after geometry optimization at the ZORA-OPBE/QZ4P level of theory in vacuum. Parts of the molecule are shown as wireframes for the sake of clarity; the dipole vector is circled in red.

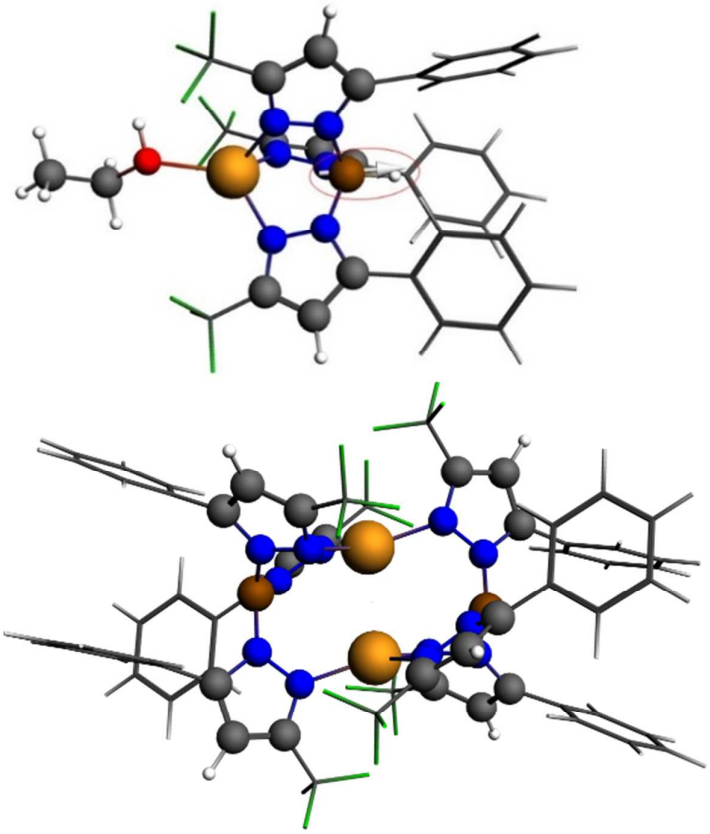

Figure S15. Projection of the structure of [Cu($Tp^{CF3,\ Ph}$)(C_2H_5OH)] (left) and [Cu($Tp^{CF3,Ph}$)]$_2$ (right) after geometry optimization at the ZORA-OPBE/QZ4P level of theory in vacuum. Parts of the molecule are shown as wireframes for the sake of clarity; the dipole vector in the ethanol complex is circled in red.

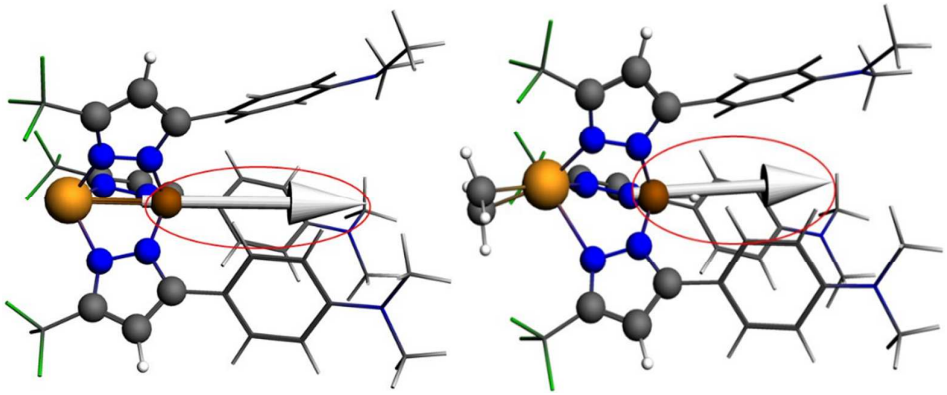

Figure S16. Projection of the structure of [Cu($Tp^{CF3,4\text{-}NMe2Ph}$)] (left) and [Cu($Tp^{CF3,4\text{-}NMe2Ph}$)(C_2H_4)] (right) after geometry optimization at the ZORA-OPBE/QZ4P level of theory in vacuum. Parts of the molecule are shown as wireframes for the sake of clarity, the dipole vectors are circled in red.

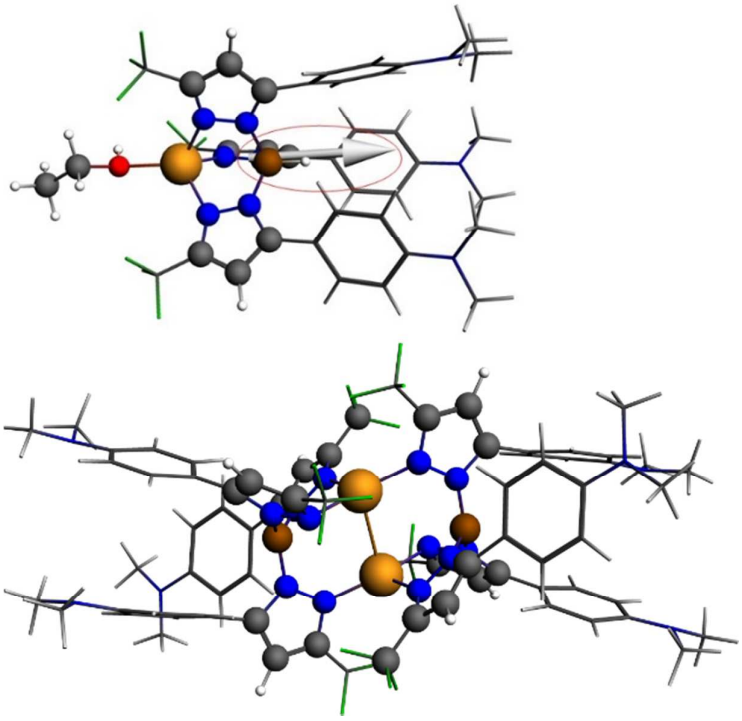

Figure S17. Projection of the structure of [Cu($Tp^{CF3,4\text{-}NMe2Ph}$)(C_2H_5OH)] (top) and [Cu($Tp^{CF3,4\text{-}NMe2Ph}$)]$_2$ (bottom) after geometry optimization at the ZORA-OPBE/QZ4P level of theory in vacuum. Parts of the molecule are shown as wireframes for the sake of clarity; the dipole vector in the ethanol complex is circled in red.